



## Development of a wide-field EMCCD camera-based alpha-particle imaging system

Sohbati, Reza; Kook, Myungho; Jain, Mayank; Thomsen, Kristina J.; Murray, Andrew S.

*Published in:*

Measurement: Journal of the International Measurement Confederation

*Link to article, DOI:*

[10.1016/j.measurement.2022.112234](https://doi.org/10.1016/j.measurement.2022.112234)

*Publication date:*

2023

*Document Version*

Publisher's PDF, also known as Version of record

[Link back to DTU Orbit](#)

*Citation (APA):*

Sohbati, R., Kook, M., Jain, M., Thomsen, K. J., & Murray, A. S. (2023). Development of a wide-field EMCCD camera-based alpha-particle imaging system. *Measurement: Journal of the International Measurement Confederation*, 206, Article 112234. <https://doi.org/10.1016/j.measurement.2022.112234>

---

### General rights

Copyright and moral rights for the publications made accessible in the public portal are retained by the authors and/or other copyright owners and it is a condition of accessing publications that users recognise and abide by the legal requirements associated with these rights.

- Users may download and print one copy of any publication from the public portal for the purpose of private study or research.
- You may not further distribute the material or use it for any profit-making activity or commercial gain
- You may freely distribute the URL identifying the publication in the public portal

If you believe that this document breaches copyright please contact us providing details, and we will remove access to the work immediately and investigate your claim.



# Development of a wide-field EMCCD camera-based alpha-particle imaging system

Reza Sohbati<sup>a,b,\*</sup>, Myungho Kook<sup>a</sup>, Mayank Jain<sup>a</sup>, Kristina J. Thomsen<sup>a</sup>, Andrew S. Murray<sup>c</sup>

<sup>a</sup> Department of Physics, Technical University of Denmark, Risø Campus, 4000 Roskilde, Denmark

<sup>b</sup> Danish Fundamental Metrology, Kogle Allé 5, 2970 Hørsholm, Denmark

<sup>c</sup> Department of Geoscience, Aarhus University, DTU Risø Campus, 4000 Roskilde, Denmark

## ARTICLE INFO

### Keywords:

Alpha particle imaging  
(EM-)CCD camera  
Thermal noise  
Cosmic noise  
Geochemistry  
Geochronology

## ABSTRACT

We demonstrate a wide-field alpha-particle imaging system based on the detection of alpha-induced scintillation light from ZnS:Ag screen using an EMCCD camera. We develop an efficient image processing algorithm to remove cosmic and thermal noise and to locate alpha particle interactions in EMCCD images. This algorithm is particularly suited to imaging low-activity samples where long image acquisition periods entail a large number of frames with no detected alpha particle. Our system has a relative counting efficiency of ~50 % compared to a PMT-based alpha counter. It can detect alpha particles at a resolution of <math><480 \mu\text{m}</math> over an imaging area of ~45 × 45 mm. We demonstrate the performance of this system by imaging a granite sample. Correlation between the resulting alpha image and the micro XRF-determined element map demonstrates that most of the alpha activity in our sample is held in dark-coloured Ba-rich veins and inclusions at mineral grain boundaries.

## 1. Introduction

Detection and measurement of ionising radiation, including alpha particles, is of primary interest in a wide range of environmental, medical and industrial applications [1]. Specifically, in environmental sciences, determining the distribution of radionuclides at micrometre scales is crucial for managing the radiation risks of uranium mining [2], radioactive waste disposal [3], radioactive dust dispersal [4], and for geochronology [5].

Various techniques have been developed for spatially resolved detection of radionuclides through the imaging of alpha particles. These include autoradiographic methods using films [6,7], storage phosphors [8,9] and micropattern gaseous detectors [10], and the imaging of alpha-induced scintillation light using position-sensitive photo-multipliers [11,12] and CCD/CMOS cameras [13,14].

In this study, we describe a wide-field instrument for the near-real-time imaging of alpha particles from samples containing low levels of natural radioactivity. The instrument is based on an Electron-Multiplied (EM) CCD camera viewing the light emitted by a silver-doped zinc sulphide (ZnS:Ag) scintillation screen when impacted by an alpha particle. We develop an efficient image processing algorithm to remove cosmic and thermal noise and to automatically locate alpha particles in EMCCD images. Such an algorithm is essential to the optimisation of image

processing time. This is especially true for low-activity samples such as geological specimens, where long exposure (and so long image acquisition periods) results in a large number of images with no detectable alpha events. We establish the detection efficiency of our imaging system by comparison with the count rate recorded by a photomultiplier tube (PMT) viewing a ZnS:Ag screen [15] (hereafter referred to as an alpha counter) and determine its resolution by imaging a synthetic radioactive sample of known geometry. We further demonstrate the performance of our system by imaging alpha particles from a granite sample and correlate the cumulative alpha particle image with the corresponding micro-XRF element map.

## 2. Hardware configuration

The instrument is made up of: (i) a light-tight sample chamber, (ii) an optical focusing lens (Schneider-Kreuznach, Xenon 25 mm f/0.95) and (iii) an EMCCD camera (Photometrics, Evolve 512) (Fig. 1). The light-tight chamber was customised by drilling an aperture on the top of an off-the-shelf aluminium box to allow the scintillation light to pass through the lens to the camera. It was tested for leakage by collecting images in the absence of a scintillator. Only electronic noise and high energy events were present. The chamber was also fitted with an adjustable sample stage enabling the imaging of samples of various

\* Corresponding author at: Danish Fundamental Metrology, Kogle Allé 5, 2970 Hørsholm, Denmark.

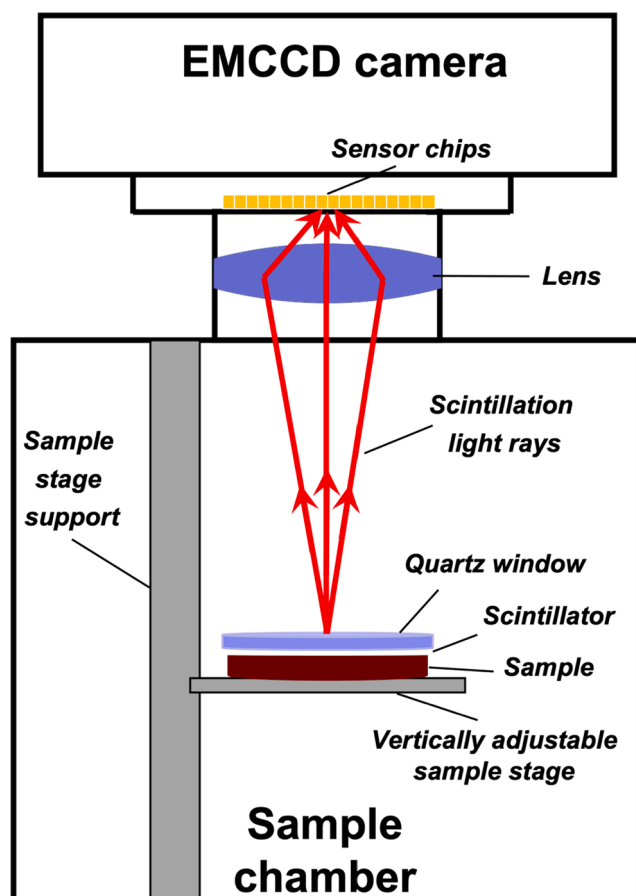


**Fig. 1.** Schematic view of the alpha particle imaging unit. The system is composed of a light-tight sample chamber with a lid, a height-adjustable sample stage, a silver-doped zinc sulphide (ZnS:Ag) scintillator, a quartz window, an optical lens and an EMCCD camera. At a distance of  $\sim 12$  cm between the sample and the lens, the instrument can image areas as large as  $\sim 45 \times 45$  mm.

heights (Fig. 1). The CCD chips were maintained at a temperature of  $-80$  °C throughout the measurements. No chip normalisation was applied as it was not deemed necessary. The EM gain of the camera was

set to 250. The raw CCD images were collected using custom software in Delphi.

The scintillation light was generated using an EJ-440 scintillator from Eljen Technology which consists of ZnS:Ag phosphor applied to a transparent polyester plastic sheet with a diameter of 50 mm and a thickness of 0.25 mm. The scintillator is placed directly on top of the sample and an optically transparent quartz window (3 mm thick,  $\varnothing$  44 mm; by Schott) is used as a weight to minimise any gap between the scintillator and the sample and the accumulation of radon and radon daughters in the airspace between the two (Fig. 1). At a distance of  $\sim 12$  cm between the lens and the scintillator, the system has an imaging area of  $\sim 45 \times 45$  mm. The minimum image acquisition time is 33 ms, but was set to 1 s (i.e. frame rate = 1 fps) in all the measurements described here.

### 3. Image processing

To develop a robust algorithm for identifying alpha particles in noisy images, we synthesised an active sample by mixing  $\sim 4$  g of reference uranium ore BL-5 (in powder form, certified by NRCAN; activity  $\sim 875$  Bq.g $^{-1}$ ) with  $\sim 8$  g of resin and casting the mixture in the shape of a disc with a diameter of 40 mm and a thickness of 3 mm (Fig. 2a). A measurement of this sample using an alpha counter with an absolute efficiency of 82 and 85 % for  $^{238}\text{U}$  and  $^{232}\text{Th}$  series, respectively [15], yielded an alpha count rate of  $\sim 25 \times 10^3$  counts per kilosecond (ks $^{-1}$ ).

Fig. 2b shows a typical CCD single frame (1 s) image from the BL-5 sample. Three types of light emitting areas are observed in this image: (i) large roundish clusters of pixels recording many photons, representing alpha events, (ii) small areas with only few pixels registering counts, typical of thermal noise [16] and (iii) dense clusters of pixels with long tails, recording many counts, characteristic of cosmic noise [17] (Fig. 2b).

To extract the spatial distribution of alpha activity making up this image, the thermal and cosmic noise need to be characterised in such a way that they can be automatically identified and removed. These interfering events do not originate from the scintillator, but are generated within the CCD sensor chip itself. To characterise these events, we measured the inherent background of the detector (i.e. with no sample or scintillator) for 1000 s (i.e. 1000 frames). We then processed these individual background images by calculating various properties of all the non-zero pixels (singular or clustered) as Regions Of Interest (ROIs) using the image processing toolbox in MATLAB. Specifically, the *area* (i.e. the number of connected pixels), the *sum intensity* (i.e. the sum of pixel

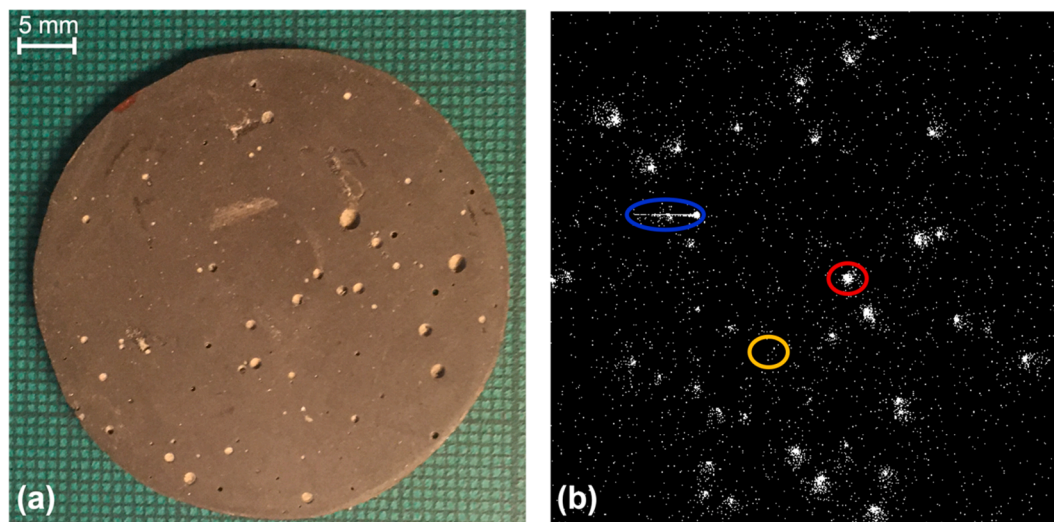


**Fig. 2.** (a) Optical image of a “hot” sample synthesised by mixing BL-5 reference uranium ore powder with resin. The sample has a mean alpha count rate of  $\sim 25 \times 10^3$  ks $^{-1}$  measured by a PM-based alpha counter. (b) A typical CCD image frame of 1 s duration from the sample shown in (a). The red, blue and yellow ovals in (b) mark an example of alpha incidence, cosmic noise and thermal noise, respectively. The scale bar in (a) applies to (b) as well.

values), the *mean intensity* (i.e. the sum of the pixel values divided by the total number of pixels), and *weighted centroid* (i.e. the centre based on both location and intensity of pixels) of each ROI were calculated.

### 3.1. Cosmic noise removal

A comparison between the ROI area versus mean intensity shows two very distinct types of clusters in the dataset (Fig. 3). Inspection of typical frames from each cluster revealed that frames with mean intensities  $<20$  only include thermal noise, while frames including ROIs with mean intensities  $>20$  have registered at least one cosmic noise event (Fig. 3). Cosmic rays measured here are essentially high-energy protons and neutrons which are expected to generate high pixel values when interacting with the CCD chip [17]. We conclude that (i) mean intensity is a robust criterion with which to distinguish between cosmic and thermal noise, and (ii) ROIs with mean intensities  $>20$  in background measurements are cosmic noise and must be removed. Approximately  $50 \text{ ks}^{-1}$  cosmic ray events are detected by our system.

### 3.2. Thermal noise removal

Further analysis of the same data shown in Fig. 3 after the removal of cosmic noise (i.e. data with mean intensities  $>20$ ) indicates that the individual thermal noise events can be registered by areas of up to 12 pixels. As a result, we regard ROIs  $< 13$  pixels in area as thermal noise and remove them. Applying this threshold may overlook some of the low-energy alpha particles, but all noise removal algorithms bear some compromise, and we consider this an acceptable trade-off. It must be noted that our system is intended for use with thick sources – by definition, some alpha particles leaving such sources will have energies approaching zero. Thus, it is inevitable that some alpha particles will generate photon counts that are comparable to thermal noise. The mathematical description of the emission of alpha particles of a given range (energy) from such thick sources is given by [18].

Fig. 4(a-c) demonstrates the performance of this frame-by-frame noise removal algorithm on a typical frame from the high activity BL-5 sample. The removal of noise (both thermal and cosmic) leaves a clear image of only alpha particles interacting with the scintillator (Fig. 4c). Frames that have no activated pixels remaining after this analysis are not included in further analysis.

The alpha event background for ZnS:Ag screens (e.g. arising from

radon in air and contamination of the scintillation screen) is typically  $<0.3 \text{ ks}^{-1}$  in a total alpha counter [15]; in our system the effective background is calculated per pixel, and is thus negligible.

### 3.3. Locating alpha interactions with the scintillator

To determine the location of the individual alpha events remaining after noise removal, we use the weighted centroid, determined by considering both the location and value of individual pixels in each ROI (Fig. 4d).

### 3.4. Determination of spatial resolution

Having removed the noise and located the alpha particles, we next determine the spatial resolution of the system. To do so, we first synthesised a sample of known geometry. This was achieved by cutting five grooves into a PMMA disc, 43 mm diameter and 5 mm thick. Grooves were 2 mm wide and 2.5 mm deep, with 5 mm spacing (Fig. 5a). Each groove was then filled with our standard mixture of BL-5 described above, and the surface was gently polished to remove any residue and to create a flat, smooth, and even surface.

We next quantified the effective pixel size of the system by capturing an optical image of a scale bar using reflected light from an LED light source filtered by a 3-mm thick Schott BG3 filter with an emission peak of 350 nm in the visible range, close to that of the ZnS:Ag scintillator (peak at 450 nm). Dividing the imaged length of the scale bar (i.e. 4.5 cm) by the total number of pixels (i.e. 512) in the corresponding dimension gives a pixel size of  $\sim 88 \mu\text{m}$  (Fig. S1).

A cumulative image ( $640 \times 10^3$  frames) of alpha events from the synthetic sample shows numerous alpha particles emitting from the grooves filled with the radioactive mixture, while there are no visible alpha particles from the PMMA substrate (Fig. 5b). Not surprisingly, the alpha activity of the BL-5 mixture within the grooves is non-uniform; some pixels have registered  $>700$  events, whereas others have recorded as few as one event only.

To determine the spatial resolution of the system (i.e. how well we can resolve two events as derived from alpha particle interactions with the scintillator), we calculated the intensity profile of each horizontal row of pixels (512 in total) in Fig. 5b. Here “intensity” refers to the total number of alpha events registered by each pixel along the profile. The average profile (red thick line in Fig. 6a) shows that the intensity is zero

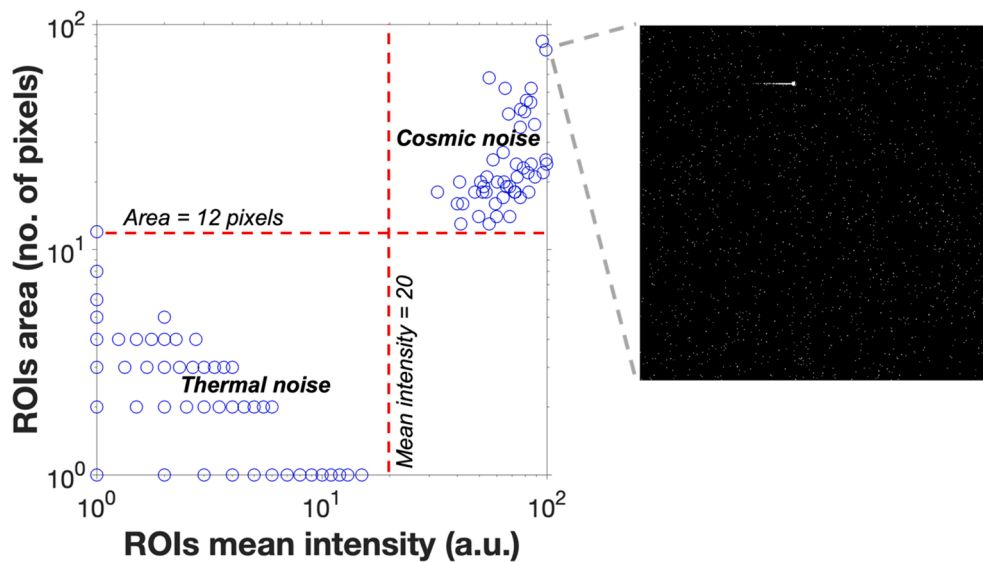
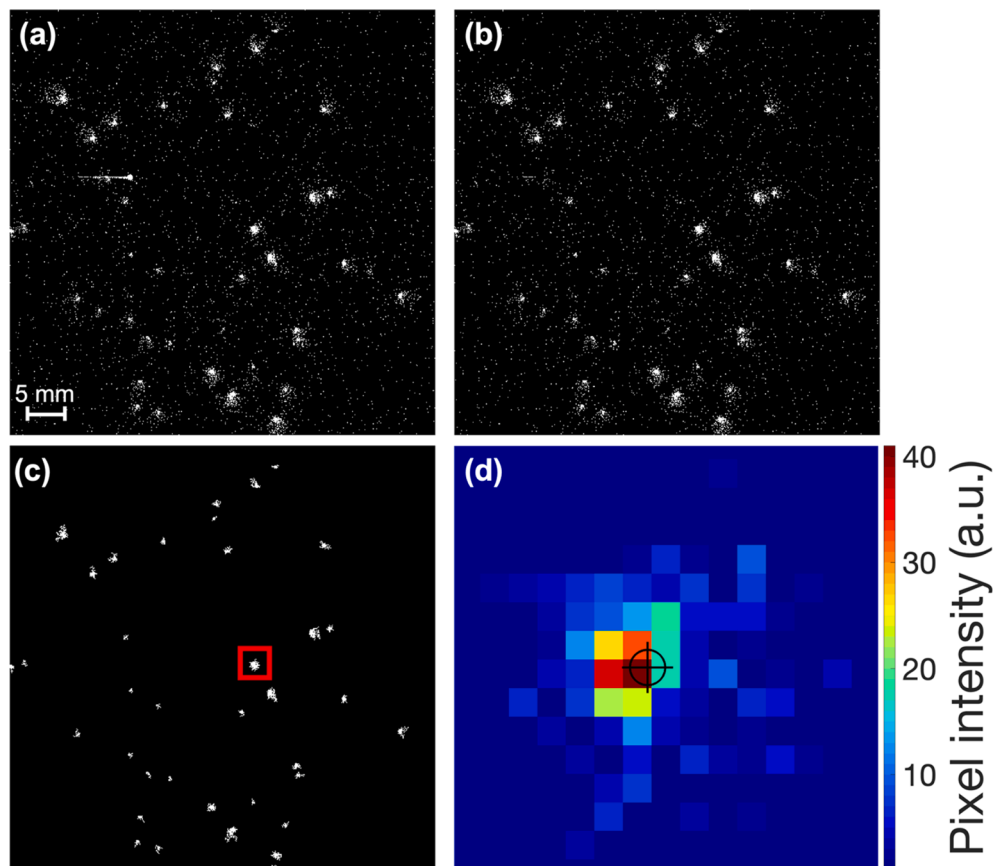
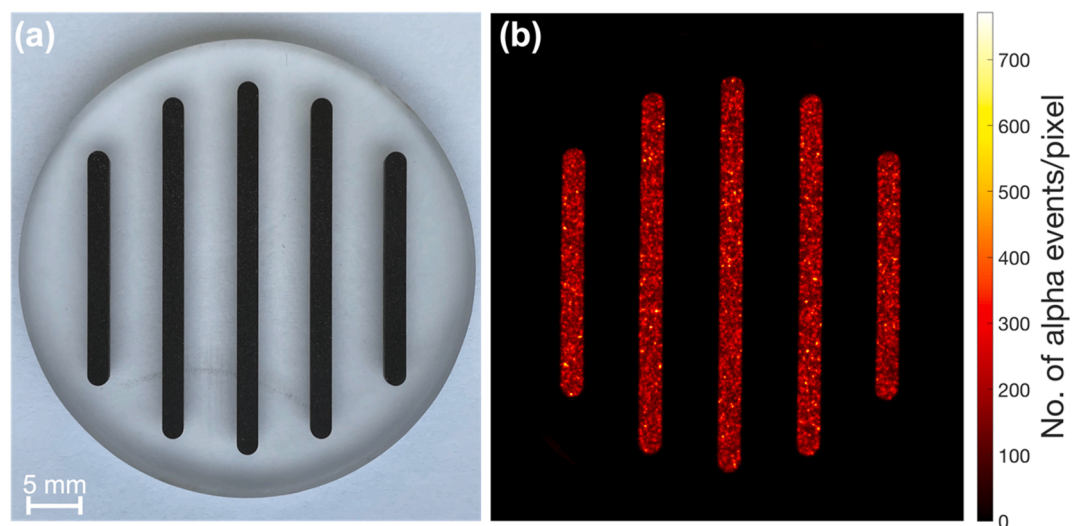


Fig. 3. Area versus mean intensity of non-zero pixels/pixel areas calculated from 1000 frames (equivalent to 1000 s) of background measurement with no scintillator. Data points with mean intensities  $>20$  belong unanimously to frames with cosmic noise, while data points with mean intensities  $<20$  are calculated from frames with thermal noise only. The largest thermal noise is 12 pixels in area.



**Fig. 4.** Performance of the noise removal algorithm. (a) A typical raw image from the custom-made BL-5 sample with alpha particles, cosmic noise and thermal noise as shown in Fig. 2b. (b) The same frame as in (a) after the removal of cosmic noise with mean intensities  $>20$ . (c) The same frame as in (a) and (b) after the removal of thermal noise  $<13$  pixels in area. (d) A close-up of a cluster of pixels representing the alpha particle enclosed by the red square in (c). The crossed circle pinpoints the weighted centroid of the cluster taken as the position of the alpha particle. The scale bar in (a) applies to (b) and (c) as well. The frame exposure time was 1 s.



**Fig. 5.** (a) Artificial sample with grooves filled with a mixture of BL-5 standard and resin. Each groove is 2 mm wide, 2.5 mm deep, and 5 mm apart from the neighbouring groove. (b) The cumulative ( $\sim 640 \times 10^3$  frames, 1 s each) alpha event image of the sample in (a). The scale bar in (a) applies to (b) as well.

near the edges of the sample, but as we approach the alpha-emitting grooves it rises, remains more or less constant over the width of the groove, and then drops back to zero in the gap between the grooves. It is noteworthy that the mean intensity is slightly higher at the centre (i.e. pixel range: 200–275) and symmetrically decreases by  $\sim 35\%$  towards the edges of the image, presumably indicating that the overall detection efficiency of the system is higher at the centre.

The rising and falling fronts of the mean intensity profile at each edge of each groove represents an edge step function (ESF). The 1st derivative

of an ESF is a line spread function whose FWHM provides an estimate of spatial resolution [19,20]. Fig. 6b shows the 1st derivative of the mean intensity profile, where the peaks mark the inflection points in the rising/falling fronts of the mean intensity profile (i.e. ESFs) in Fig. 6a. The FWHM of the peaks ranges from 5 to 5.7 pixels with an average of 5.44 pixels ( $n = 10$ ). No systematic trend is observed in the size of the FWHM with the relative location of the corresponding edge within the imaging area, implying that the spatial resolution over the entire imaging area is relatively uniform (Fig. 6b). Multiplying the average of 5.44 pixels by

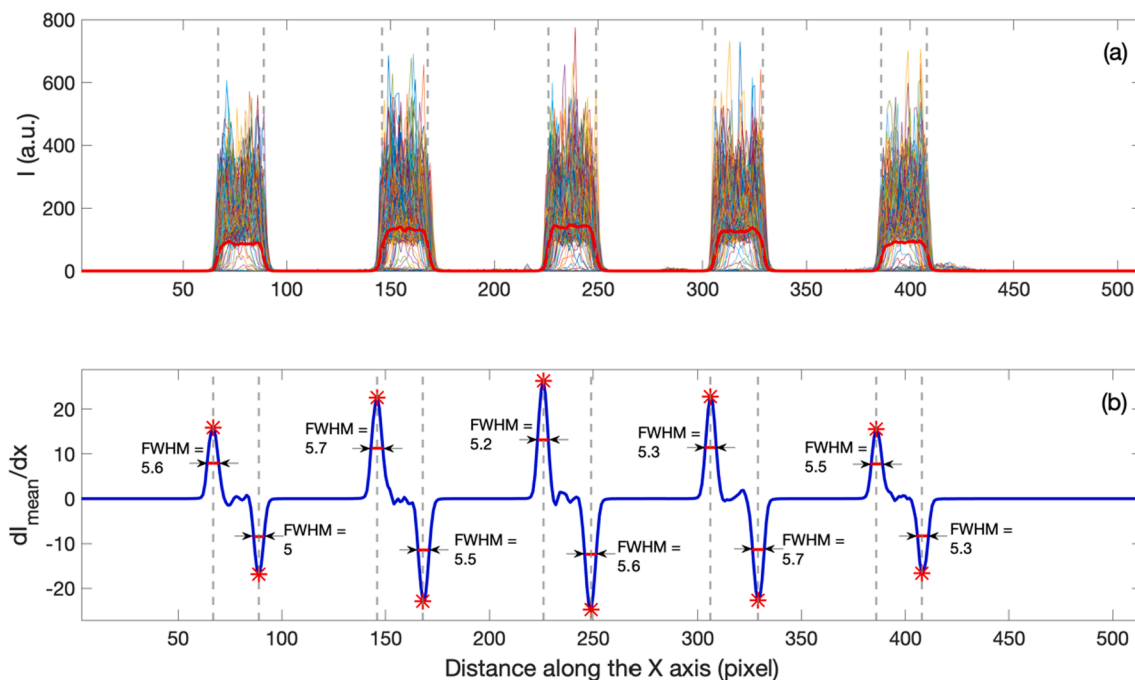


**Fig. 6.** Determination of spatial resolution. (a) The intensity profiles (i.e. the number of detected alpha events per pixel) along the horizontal pixel rows (512 in total) of the cumulative alpha event image shown in Fig. 5b. (b) The 1st derivative of the average profile shown as the thick red line in (a). The minimum and maximum peaks denoted by stars represent the inflection points in the mean profile. The FWHM is an estimate of spatial resolution.

the pixel size (i.e.  $88 \mu\text{m}$ ) determined above gives an apparent spatial resolution of  $\sim 480 \mu\text{m}$  for our alpha particle imaging unit. We deem this value as an upper limit to the spatial resolution, because it includes the effects of non-uniform activity within the grooves. This is particularly visible in the variability in the rise and fall of the individual pixel rows at the groove edges (Fig. 6a).

### 3.5. Counting efficiency

As mentioned above, the measurement of the BL-5 disc sample (Fig. 2a) on the alpha counter yielded a mean count rate of  $\sim 25 \times 10^3 \text{ ks}^{-1}$ . To evaluate the efficiency of our system, we imaged the same sample and obtained a mean count rate of  $\sim 12.6 \times 10^3 \text{ ks}^{-1}$  over the entire imaging area implying a relative counting efficiency of  $\sim 50\%$  compared to the alpha counter with an absolute counting efficiency of  $\sim 42\%$  (Aitken, 1985; Appendix J). A lower counting efficiency of the imaging system compared to that of a PMT-based alpha counter is expected because of the inevitably smaller numerical aperture of the focussed imaging system (in the alpha counter, the scintillator is within 3 mm of the front face of the PMT), and because of the reduced detection efficiency of the camera towards the edges of the imaging area (due to lens aberrations). This results in a greater number of alpha events falling below the effective detection threshold in the imaging system.

To estimate the efficiency of the imaging unit in the central part of the imaging area, where the adverse effect of lens aberration is smaller, we restricted the counting area by cropping the scintillator to  $10 \times 10 \text{ mm}$ , and placed it at the centre of the sample and thus of the imaging area (Fig. S2). We then remeasured this new sample-scintillator configuration using both the alpha counter and our imaging system, so the size of the light-emitting area was identical in both measurements (Fig. S2). The mean alpha count rates from the counter and the camera were  $\sim 2.1 \times 10^3$  and  $1.8 \times 10^3 \text{ ks}^{-1}$ , respectively, suggesting a relative efficiency of  $\sim 86\%$  for the imaging system compared to that of the alpha counter.

## 4. Alpha image of a granite sample and correlation with element map

To illustrate the application of our system in environmental geochemistry and geochronology, we measured the fine-polished surface of a granite disc, 44 mm diameter and 5 mm thick (Fig. 7a). Fig. 7b shows a cumulative alpha image of the same disc measured over a period of  $\sim 8$  days during which  $\sim 9.7 \times 10^3$  alpha particles were detected. From this image, it is clear that the majority of alpha particles are emitted from a few hotspots within the sample, while other events seem to happen randomly almost everywhere across the sample surface.

To investigate the origin of the emitted alpha particles, we mapped various elements in the sample using an M4 TORNADO micro-XRF ( $\mu\text{XRF}$ ). This instrument is not sensitive enough to detect heavy alpha-emitting radioelements such as uranium and thorium and their progeny, because these are only present in trace amounts of only few ppm in most natural minerals. It can however provide high resolution maps (X-ray beam size is  $< 20 \mu\text{m}$ ) of many other major and minor elements such as Si, K, Ca and Fe, with which U and Th are associated in various mineral structures.

Quartz and feldspars, which are the major constituent minerals of our granite sample, do not usually contain any significant amount of alpha activity [21,22]. We expect the imaged alpha particles to originate mainly from outside quartz and feldspar grains, i.e. from other minerals and from grain boundaries. To test this hypothesis, we first made a composite map of Si, K, Ca and Fe (Fig. 7c). Si represents mainly quartz, while K and Ca are the key elements of alkali and plagioclase feldspars, respectively (Fig. 7c). We then derived the element boundaries as a proxy for mineral boundaries (Fig. 7d).

In order to compare the alpha image with the grain boundary map, they must first be aligned. The geometric transformation required for the alignment was derived by aligning the optical images captured by the EMCCD camera and the inbuilt camera in the  $\mu\text{XRF}$  using the *imregcorr* function and applied through the *imwarp* function in MATLAB. The *imregcorr* function is based on the method by [23] which provides exact matching for translational and rotational movements, and a scaling match down to the third decimal place.

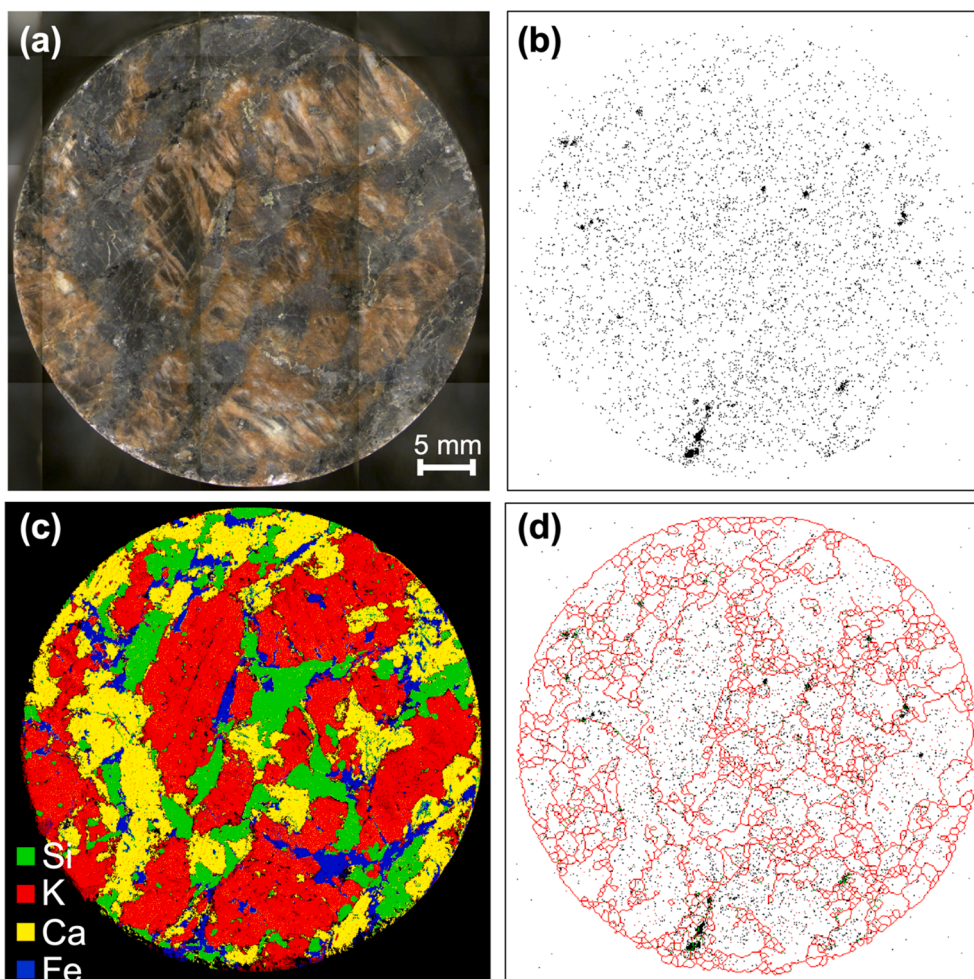


**Fig. 7.** (a) Optical image of the polished surface of the granite sample. (b) The cumulative image of alpha events from the same sample in (a) collected for a period of ~8 days, during which  $\sim 9.7 \times 10^3$  events were detected. (c) The micro-XRF map of major elements in the granite surface. (d) The boundary map of major elements in (c) overlaid on the alpha-event map in (b). The green areas highlight some of the spots where the two maps overlap.

The superimposition of the geometrically transformed alpha event image on the grain boundary map indicates that many of the alpha emitting hotspots do indeed seem to occur on the grain boundaries, consistent with the hypothesis that that U and Th tend to localise in the dark-coloured material such as veins and inclusions found at grain boundaries [6,24]. In addition, all larger grains do show some internal

alpha activity (Fig. 7d), while a few smaller grains show no significant alpha activity (Fig. 7d).

Further comparison between individual maps of minor elements and the alpha image revealed an apparent correlation between the Ba map and the alpha image; a significant number of hotspots on the alpha image correspond to Ba-rich areas on the Ba map (Fig. 8). There are

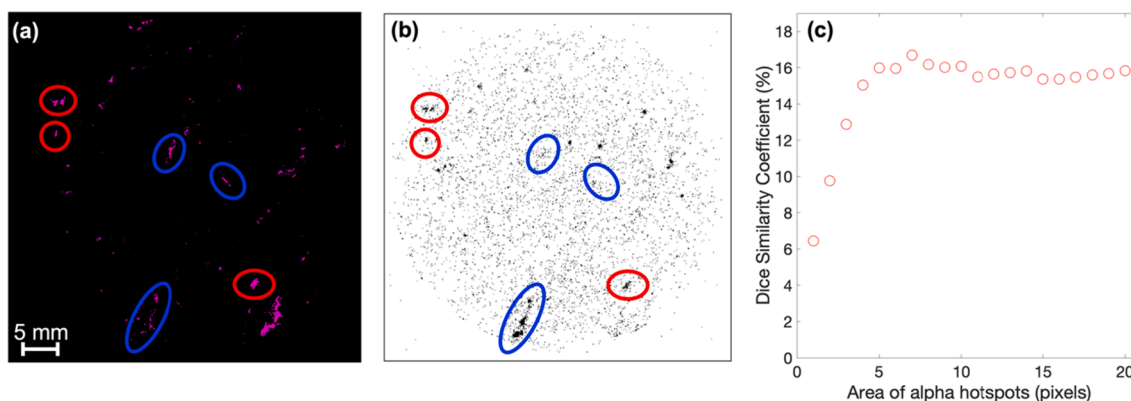


**Fig. 8.** Comparison between (a) Ba map and (b) alpha-event image from the granite sample. The red circles and ovals enclose some of the areas where the Ba map is similar to the alpha image, while the blue ovals highlight some of the dissimilarities. (c) Dice similarity coefficient between the Ba map and the alpha-event image. The similarity is ~6% when all the alpha events are included and gradually rises to ~16% as the area of the alpha emitting spots that are included in the comparison is increased to 5 pixels. For alpha hotspots that are >5 pixels, the Dice coefficient remains more or less constant at ~16%. The scale bar in (a) applies to (b) as well.

nevertheless some areas where the apparent correlation is not as obvious. This variability in correlation may partly arise from the fact that the depth resolutions of the alpha image and the element map are three orders of magnitude different. Alpha particles originate from the top few  $\mu\text{m}$  of the sample, but the Ba map is generated by X-rays with a critical penetration depth of a few millimetres for Ba K lines [25].

To quantify the apparent similarity between the alpha image and the Ba map, we calculated the Sørensen-Dice coefficient [26,27]. In our context, this coefficient is equal to twice the number of light emitting pixels that are common to both images divided by the sum of the number of light emitting pixels in each image. We first derived the coefficient including all the pixels in the alpha image (even those that have registered only one alpha event) and obtained  $\sim 6\%$  similarity between the alpha image and the Ba map. But as we focused on alpha hotspots by increasing the area of the regions of interest for comparison, the similarity increased to  $\sim 16\%$  at 5-pixel area and remained more or less constant at larger areas (Fig. 8c). We thus infer that there is  $\sim 16\%$  similarity between alpha hotspots and Ba-rich areas in our granite sample.

The same similarity analysis was carried out for other elements. Table 1 summarises the results for five elements whose maps are found to be most similar to the alpha hotspots (i.e.  $>5$  pixels in area) image. After Ba, the Zr map with a similarity of  $\sim 6\%$  is the most similar to the alpha hotspots image (Table 1). Zr is known to be associated with U and Th in the form of zircon as a common mineral in granitic rocks. Mn, Fe and Mg were the only other elements whose maps had a similarity  $\geq 1\%$  compared to the alpha hotspot image.

## 5. Discussion and conclusion

Although we used a highly sensitive EMCCD camera for detecting the alpha particle-induced scintillation light in this study, we believe that most ordinary CCD cameras have the required sensitivity to detect similar levels of light output at comparable speeds (i.e. 1 fps), rendering them as suitable in similar applications.

Originally, we were hoping to detect beta particles with our system as well. We investigated the possibility by measuring a  $^{99}\text{Tc}$  beta source and a sample of potassium sulphate in powder form with both a ZnS:Ag screen and a BC-422 plastic beta scintillator from Saint-Gobain. But, in no case were we able to detect any light from beta particles using our optics and detection thresholds. In general, the lower energy of beta particles and the lower sensitivity of beta scintillators make the detection of beta particles more difficult compared to that of alphas.

We present a new alpha particle imaging instrument based on CCD imaging of scintillation light generated by the impact of alpha particles on a ZnS:Ag scintillator. The images are processed using a robust algorithm that successfully eliminates thermal and cosmic noise, identifies the alpha particles and determines their location at a resolution of  $<480\ \mu\text{m}$  over an imaging area of  $\sim 45 \times 45\ \text{mm}$ . The counting efficiency of our imaging system is  $\sim 50\%$  relative to a total alpha counter. The relative counting efficiency increases to  $\sim 86\%$  when imaging is limited to an area of  $100\ \text{mm}^2$  at the centre of the image, where lens aberration effects are minimal. We consider our system as wide-field, because the total imaging area of  $2025\ \text{mm}^2$  achieved here is significantly larger than the reported field of view for comparable CCD-based setups e.g. [14,28].

Our image processing algorithm is especially useful for imaging low-activity samples such as geological specimens for which making a clear alpha image requires long acquisition times entailing a very large number of noisy images with no alpha events. Our approach can detect and ignore such frames in a near-real-time mode, significantly improving final image processing time. Our camera can operate with frame rates as high as  $33\ \text{ms}^{-1}$ . In high activity samples this processing ability will allow the separation of U and Th using the pairs counting technique [15].

It is noteworthy that although the mathematical filters designed and

**Table 1**

The Dice similarity coefficient (DSC) for five element maps that were most similar to the map of alpha hotspots (i.e.  $>5$  pixels) in the granite surface.

Element	DSC (%)
Ba	16
Zr	6
Mn	4.5
Fe	1.5
Mg	1

implemented here are primarily developed for detecting alpha particles from natural emitters (U, Th and progeny) and removing thermal and cosmic noise, they can, in principle, identify any other source of radiation that gives rise to similar signals or noise, and detect or remove them accordingly. For instance, we presume that gamma rays interact with the CCD chips in a similar manner to cosmic rays. In that case, the filter for cosmic rays proposed here should be able to remove gamma rays as well. Obviously, if a radiation source gives rise to a signal or noise that is very different in shape and intensity than those characterised by the filters applied in this study, then the filters must be adjusted or new filters must be defined and implemented to detect or remove them, respectively.

The value of this new instrument has been illustrated by imaging alpha emission from a granite surface. This image indicates that the alpha activity is heterogeneously distributed and mostly held in the dark-coloured veins and inclusions at mineral grain boundaries. A further comparison between the alpha image and various element maps revealed a similarity of  $\sim 16\%$  between the alpha hotspots and the distribution of Ba, suggesting a strong mineralogical association between Ba and alpha-emitting U and Th in our sample.

Information on the spatial distribution of radioactivity is of considerable importance in the interpretation of dose distributions [29], and luminescence-depth profiles in trapped charge geochronometry [30]. Images of alpha distributions can also be used to guide and evaluate microdosimetry modelling and simulations. When combined with  $\mu\text{XRF}$  (for K distributions) the alpha activity map has the potential to allow grain-specific radiation dose rates to be derived.

## Declaration of Competing Interest

The authors declare that they have no known competing financial interests or personal relationships that could have appeared to influence the work reported in this paper.

## Data availability

Data will be made available on request.

## Acknowledgments

The authors would like to thank Henrik Olesen for sample preparation and Soren Vig Dalsgaard for manufacturing the mechanical parts. Dr Alastair Cunningham is acknowledged for assistance with the alpha counter setup.

## Appendix A. Supplementary material

Supplementary data to this article can be found online at <https://doi.org/10.1016/j.measurement.2022.112234>.

## References

- [1] G.F. Knoll, Radiation Detection and Measurement, John Wiley & Sons, 2010.

- [2] A. Abdelouas, Uranium mill tailings: geochemistry, mineralogy, and environmental impact, *Elements* 2 (2006) 335–341.
- [3] T.T. Vandergraaf, D.R.M. Abry, C.E. Davis, The use of autoradiography in determining the distribution of radionuclides sorbed on thin sections of plutonic rocks from the Canadian Shield, *Chem. Geol.* 36 (1-2) (1982) 139–154.
- [4] M.J. Heard, R.D. Wiffen, Alpha track autoradiography of sub-micron aerosol particles with the electron microscope, *Nature* 219 (5160) (1968) 1245–1248.
- [5] M. Walker, *Quaternary Dating Methods*, John Wiley and Sons, 2005.
- [6] C. Schmidt, D. Rufer, F. Preusser, M. Krbetschek, A. Hilgers, The assessment of radionuclide distribution in silex by autoradiography in the context of dose rate determination for thermoluminescence dating, *Archaeometry* 55 (2013) 407–422.
- [7] C.A. Kalnins, N.A. Spooner, M.J. Clarke, D. Ottaway, Alpha particle autoradiography for high spatial resolution mapping of radionuclides, *J. Environ. Radioact.* 197 (2019) 9–15.
- [8] J.M. Cole, J. Nienstedt, G. Spataro, E.T. Rasbury, A. Lanzirrotti, A.J. Celestian, M. Nilsson, G.N. Hanson, Phosphor imaging as a tool for in situ mapping of ppm levels of uranium and thorium in rocks and minerals, *Chem. Geol.* 193 (1-2) (2003) 127–136.
- [9] B.o. Chen, W. Zhuo, Y. Kong, Fading characteristics of alpha radiation signals stored in an imaging plate, *J. Nucl. Sci. Technol.* 48 (8) (2011) 1158–1162.
- [10] P. Sardini, A. Angileri, M. Descostes, S. Duval, T. Oger, P. Patrier, N. Rividi, M. Siitari-Kauppi, H. Toubon, J. Donnard, Quantitative autoradiography of alpha particle emission in geo-materials using the Beaver™ system, *Nucl. Instrum. Methods Phys. Res., Sect. A* 833 (2016) 15–22.
- [11] S. Yamamoto, T. Iida, A position-sensitive alpha detector using a thin plastic scintillator combined with a position-sensitive photomultiplier tube, *Nucl. Instrum. Methods Phys. Res., Sect. A* 418 (2-3) (1998) 387–393.
- [12] S. Yamamoto, H. Ishibashi, Development of a three-layer phoswich alpha-beta-gamma imaging detector, *Nucl. Instrum. Meth. Phys. Res. Sect. A: Accel. Spectromet. Detect. Assoc. Equip.* 785 (2015) 129–134, <https://doi.org/10.1016/j.nima.2015.02.062>.
- [13] B.W. Miller, S.J. Gregory, E.S. Fuller, H.H. Barrett, H.B. Barber, L.R. Furenlid, The iQID camera: an ionizing-radiation quantum imaging detector, *Nucl. Instrum. Methods Phys. Res., Sect. A* 767 (2014) 146–152, <https://doi.org/10.1016/j.nima.2014.05.070>.
- [14] S. Yamamoto, Y. Hirano, K. Kamada, A. Yoshikawa, Development of an ultrahigh-resolution radiation real-time imaging system to observe trajectory of alpha particles in a scintillator, *Radiat. Meas.* 134 (2020), 106368.
- [15] M.J. Aitken, *Thermoluminescence Dating*, 1985. Academic Press. pp. 359.
- [16] R. Widenhorn, M.M. Blouke, A. Weber, A. Rest, E. Bodegom, Temperature dependence of dark current in a CCD, in: *Sensors and Camera Systems for Scientific, Industrial, and Digital Photography Applications III*, SPIE, 2002, pp. 193–201.
- [17] T.S. Saoud, S. Moindjie, D. Munteanu, J.-L. Aufran, Natural radiation events in CCD imagers at ground level, *Microelectron. Reliab.* 64 (2016) 68–72.
- [18] R.C. Turner, J.M. Radley, W.V. Mayneord, The alpha-ray activity of human tissues, *Br. J. Radiol.* 31 (368) (1958) 397–406.
- [19] P.W. Nugent, J.A. Shaw, M. Kehoe, C. Smith, T. Moon, R. Swanson, Measuring the modulation transfer function of imaging spectrometers at infinite focus with roof-line images, in: *Imaging Spectrometry XII*, SPIE, 2007, pp. 216–223.
- [20] B.W. Miller, S.H.L. Frost, S.L. Frayo, A.L. Kenoyer, E. Santos, J.C. Jones, D.J. Green, D.K. Hamlin, D.S. Wilbur, D.R. Fisher, J.J. Orozco, O.W. Press, J.M. Pagel, B. M. Sandmaier, others, Quantitative single-particle digital autoradiography with  $\alpha$ -particle emitters for targeted radionuclide therapy using the iQID camera, *Med. Phys.* 42 (7) (2015) 4094–4105.
- [21] V. Mejdahl, Internal radioactivity in quartz and feldspar grains, *Ancient TL* 5 (1987) 10–17.
- [22] D. Vandenberghe, F.D. Corte, J.-P. Buylaert, J. Kučera, P.V. den Haute, On the internal radioactivity in quartz, *Radiat. Meas.* 43 (2008) 771–775, <https://doi.org/10.1016/j.radmeas.2008.01.016>.
- [23] B.S. Reddy, B.N. Chatterji, An FFT-based technique for translation, rotation, and scale-invariant image registration, *IEEE Trans. Image Process.* 5 (8) (1996) 1266–1271.
- [24] C. Schmidt, T. Pettko, F. Preusser, D. Rufer, H.U. Kasper, A. Hilgers, Quantification and spatial distribution of dose rate relevant elements in silex used for luminescence dating, *Quat. Geochronol.* 12 (2012) 65–73.
- [25] P.J. Potts, O. Williams-Thorpe, P.C. Webb, The bulk analysis of silicate rocks by portable X-ray fluorescence: effect of sample mineralogy in relation to the size of the excited volume, *Geostand. Newslett.* 21 (1997) 29–41.
- [26] L.R. Dice, Measures of the amount of ecologic association between species, *Ecology* 26 (1945) 297–302.
- [27] T.A. Sørensen, A method of establishing groups of equal amplitude in plant sociology based on similarity of species content and its application to analyses of the vegetation on Danish commons, *Biol. Skar.* 5 (1948) 1–34.
- [28] Y. Morishita, S. Kurosawa, A. Yamaji, M. Hayashi, M. Sasano, T. Makita, T. Azuma, Plutonium dioxide particle imaging using a high-resolution alpha imager for radiation protection, *Sci. Rep.* 11 (2021) 1–11.
- [29] R.P. Nathan, P.J. Thomas, M. Jain, A.S. Murray, E.J. Rhodes, Environmental dose rate heterogeneity of beta radiation and its implications for luminescence dating: monte Carlo modelling and experimental validation, *Radiat. Meas.* 37 (2003) 305–313, [https://doi.org/10.1016/s1350-4487\(03\)00008-8](https://doi.org/10.1016/s1350-4487(03)00008-8).
- [30] B. Guralnik, R. Sohbaty, *Fundamentals of luminescence photo-and thermochronometry*, in: *Advances in Physics and Applications of Optically and Thermally Stimulated Luminescence*, World Scientific, 2019, pp. 399–439.